The Effects of Surface Reflection on Estimating the Vertical Temperature–Humidity Distribution from Spectral Infrared Measurements

YOURI PLOKHENKO*

Research Center "Planeta," ROSHYDROMET, Moscow, Russia

W. PAUL MENZEL

NOAA/NESDIS, Madison, Wisconsin

(Manuscript received 15 June 1998, in final form 5 March 1999)

ABSTRACT

To improve the accuracy of vertical profiles of temperature and moisture retrieved from infrared spectral measurements, the surface emissivity must be accounted for in the solution of the inverse problem (based upon the radiative transfer equation). A model that accounts for the emission and reflection on the lower atmospheric boundary and an algorithm of solution are presented. Results using spectral measurements from an airborne radiometer over land surfaces are discussed. The solution of the inverse problem includes the surface emissivity, the surface temperature, and the vertical temperature–humidity profile. It is shown that accounting for the surface emissivity in the solution of the inverse problem substantially and positively changes the meteorological profiles.

1. Introduction

One of the objectives of meteorological remote sensing is to assess the temperature–humidity distribution of the surface–atmosphere system. The quantitative estimation of these parameters is based upon the numerical solution of the radiative transfer equation wherein contributions to the measured radiance from the observed system are modeled. The model must account for emissions from both the earth's surface and the atmosphere. How well this accounting is done plays a crucial role in the accuracy of the inverse solution. The primary goal of this work is to demonstrate the importance of accounting for the variations of surface emissivity in meteorological remote sensing so as to improve the defined temperature–humidity profiles when using infrared spectral measurements (IR).

The emissivity must be included in the solution of the inverse problem for three reasons.

1) Even small emissivity variations cause measurable changes in infrared radiance; the amplitude (dimensioned) of the differential of the radiance with respect to the emissivity variation is comparable to or even larger than the amplitudes (dimensioned) of the differential of the radiance with respect to the variations of the temperature–humidity vertical distribution. This effect is because the amplitude (nondimensioned) of the functional derivative of radiance with respect to the emissivity is at least two orders of magnitude larger than the corresponding amplitudes (nondimensioned) of the functional derivatives with respect to the temperature and moisture vertical profiles.
2) Modern satellite meteorological remote sensing instruments are very sensitive, with a relative accuracy of approximately 0.2 K. Disregarding the spectral–spatial variations of emissivity in the radiative transfer model (in the atmospheric "window" spectral channels) magnifies the errors by at least a factor of 3–5. Modeling errors, reinforced by the instability of the solution, can reduce the accuracy of the results drastically. To realize the measurement potential, an appropriate radiative transfer model that accounts for surface emissivity must be used.
3) The different kinds of surface cover, with different surface optical properties and extremely high spatial and temporal variations, restrict the use of a priori estimates of the surface effects. Therefore, the direct evaluation of emissivity is a simpler and more effective approach for modeling.

The importance of this work lies in the fact that the

* Current affiliation: Cooperative Institute for Meteorological Satellite Studies, University of Wisconsin—Madison, Madison, Wisconsin.

Corresponding author address: Youri Plokhenko, Cooperative Institute for Meteorological Satellite Studies, University of Wisconsin—Madison, 1225 W. Dayton St., Madison, WI 53706.
E-mail: YouriP@ssec.wisc.edu

current operational version of the inversion algorithms for Geostationary Operational Environmental Satellite (GOES) data processing does not account for the effects of surface emissivity variations; it uses a graybody emissivity of 0.98 for sea surfaces and 0.96 for land surfaces (Hayden 1988).

This paper consists of two parts. The first part contains short descriptions of the measurement model, the statement of the inverse problem, and the algorithm of the solution. The second part contains a description and analysis of the results of the interpretation of IR spectral measurements.

2. Measurement model, description of the problem, and the algorithm of estimation

The physical model of measurements and the mathematical basis for the algorithms developed for retrieving temperature and moisture profiles while accounting for the surface emissivity are described in this section.

The radiative transfer equation (RTE) that describes aircraft measurement of the outgoing thermal radiance for the cloud-free azimuthally homogeneous atmosphere can be written as

$$\tilde{J}(\theta) = \underbrace{\varepsilon(\theta)B(T_s)\tau_s(\theta) + \int_{\tau_s(\theta)}^{1} B[T(p)]\, d\tau\,(p,\, \theta)}_{\text{(I)}} + \underbrace{[1 - \varepsilon(\theta)]\tau_s(\theta)\tau_s(\vartheta^*) \int_{\tau_s(\vartheta^*)}^{1} B[T(p)]\tau^{-2}(p,\, \vartheta^*)\, d\tau\,(p,\, \vartheta^*)}_{\text{(II)}} + \xi, \tag{1}$$

where $\tilde{J}(\theta)$ is the measured radiance at the angle of incidence θ, $\varepsilon(\theta)$ is the effective hemispherical directional emissivity of the surface at zenith angle θ (Nicodemus 1965), $B(\ )$ is the Planck function, T_s is the surface temperature, $T(p)$ is the temperature at pressure p, $\tau(p,\, \theta)$ is the transmittance from pressure p to the top of the atmosphere in a given spectral interval at zenith angle θ, subscript s designates the value of any parameter on the surface level, ϑ^* is the effective angle of incidence of downwelling radiance, and ξ is an error of the measurement. The solar radiance is disregarded in (1); therefore, (1) is valid for daytime conditions for measurement wavelengths longer then 4.5 μm.

The terms marked as (I) and (II) in (1) describe the upwelling and downwelling reflected radiation, respectively. The transmittance is considered to be a known function of the atmospheric temperature $T(p)$ and humidity $Q(p)$ profiles. In (1), the downwelling and upwelling transmittance functions are related as follows: $\tau_{\downarrow}(p,\, \theta) = \tau_{\uparrow}(p_s,\, \theta)/\tau_{\uparrow}(p,\, \theta)$.

The effective emissivity of the scene observed in the radiometer field of view (FOV) is understood to be given by

$$\left.\begin{aligned} \varepsilon(\theta) &= \frac{\displaystyle\int_0^1 \varepsilon(\theta,\, \beta)B[T_s(\beta)]\Psi(\beta)\, d\beta}{B(T_s)} \\ T_s &= \int_0^1 T_s(\beta)\Psi(\beta)\, d\beta \end{aligned}\right\}, \tag{2}$$

where $\varepsilon(\theta,\, \beta)$ is the hemispherical directional emissivity of surface type β, which occupies fraction $\Psi(\beta)$ within the FOV and has temperature $T_s(\beta)$; and T_s is an averaged surface temperature within the FOV.

The effective angle of incidence ϑ^* of the downwelling radiance $J_{\downarrow}(\vartheta^*)$ is understood as

$$J_{\downarrow}(\vartheta^*) = \frac{\displaystyle\int_0^{\pi/2}\int_0^1 J_{\downarrow}(\vartheta)r(\theta,\, \vartheta,\, \beta)\Phi(\theta,\, \beta)\Psi(\beta)\cos(\vartheta)\sin(\vartheta)\, d\beta\, d\vartheta}{\displaystyle\int_0^{\pi/2}\int_0^1 r(\theta,\, \vartheta,\, \beta)\Phi(\theta,\, \beta)\Psi(\beta)\cos(\vartheta)\sin(\vartheta)\, d\beta\, d\vartheta}. \tag{3}$$

Here, $r(\theta,\, \vartheta,\, \beta)$ is a bidirectional reflectance function of β described by a surface shape distribution function $\Phi(\theta,\, \beta)$ (Beckmann and Spizzchino 1963; Nicodemus 1965; Hapke 1993). The product $\Phi(\theta,\, \beta)\Psi(\beta)$ describes

the composite structure of the surface within the FOV. It follows that ϑ^* is a function of wavelength.

In (1) the relation analogous to Kirchhoff's law was used so that

$$\left.\begin{aligned} r(\theta) &= 1 - \varepsilon(\theta) \\ r(\theta) &= 2\pi \int_0^{\pi/2} \int_0^1 r(\theta, \vartheta, \beta)\Phi(\theta, \beta)\Psi(\beta) \cos(\vartheta) \sin(\vartheta)\, d\beta\, d\vartheta \end{aligned}\right\}. \tag{4}$$

This result follows from the requirement of radiance constancy in isothermal conditions. In (1) the surface optical effects are described by both $\varepsilon(\theta)$ and ϑ^*, but $\varepsilon(\theta)$ dominates. The functional derivative of the radiance with respect to the effective angle of incidence will be approximately three orders less than the corresponding derivative with respect to the effective emissivity.

To bound the inverse problem in (1), a priori information is required for the spectral and geometrical characteristics of the effective emissivity $\varepsilon(\theta)$. In (1) the geometrical characteristics of $\varepsilon(\theta)$ are implicitly defined by the angle ϑ^*. We assume the condition $\vartheta^* = \theta$; in other words, the traditional ''specular reflection model'' is used. A form of spectral dependence of emissivity is assumed to be known. The spectrum is partitioned into intervals within which the surface is considered to be a graybody. Thus, (1) contains the following sought-for parameters: the spectral profile of effective emissivity $\varepsilon(\theta)$, the surface temperature T_s, the temperature profile $T(p)$, and the moisture profile $Q(p)$.

The inverse solution of (1) is an ill-posed problem (Fredholm's equation of the first kind). To be solved numerically, it must be regularized, that is, the initial problem (1) is approximated by a well-posed problem whose solution is unique, stable, and corresponds in some sense to the solution of the initial problem (Tikhnov and Arsenin 1977). It can be shown that statistical estimators best correspond to the properties of (1). The minimum variance estimator (Rao 1965) is considered. Constructing the estimates of the desired parameters $\mathbf{x}$ and ε, we suggest that the parameters in (1) satisfy the following conditions:

1) $\mathbf{x}$ is a random value (vector) that has statistical characteristics so that the average $\overline{\mathbf{x}} = 0$ and the covariance matrix $\overline{\mathbf{x}\mathbf{x}^{\mathrm{T}}} = \mathbf{R}$ (the overbar denotes the mathematical expectation);
2) $\boldsymbol{\xi}$ is a random value (vector) that has statistical characteristics so that the average $\overline{\boldsymbol{\xi}} = 0$ and the covariance matrix $\overline{\boldsymbol{\xi}\boldsymbol{\xi}^{\mathrm{T}}} = \mathbf{S}_{\xi}$, and $\boldsymbol{\xi}$ does not correlate with $\mathbf{x}$ since $\overline{\boldsymbol{\xi}\mathbf{x}^{\mathrm{T}}} = 0$; and
3) ε is a control parameter in a known interval of interest.

A linearized model of measurement then can be written as

$$\mathbf{f}(\varepsilon) = \mathbf{A}(\varepsilon)\mathbf{x} + \boldsymbol{\xi}, \tag{5}$$

where $\mathbf{f}(\varepsilon)$ designates a measurement variation vector, and $\mathbf{A}(\varepsilon) = \mathbf{A}[\mathbf{J}(\varepsilon)]$ is a matrix of the algebraic system that approximates (1), where rows indicate wavelength and columns indicate pressure. The matrix $\mathbf{A}(\varepsilon)$ can be represented in the form

$$\begin{aligned} \mathbf{A}(\varepsilon) &= \mathbf{A}[\mathbf{J}(\varepsilon)] = \mathbf{A}[\mathbf{J}_b + (1 - \varepsilon)\mathbf{J}_r] \\ &= \mathbf{A}(\mathbf{J}_b) + (1 - \varepsilon)\mathbf{A}(\mathbf{J}_r) = \mathbf{A}(\varepsilon) \\ &= \mathbf{A} + (1 - \varepsilon)\mathbf{G}, \end{aligned} \tag{6}$$

where $\mathbf{A} = \mathbf{A}(\mathbf{J}_b)$ designates the linear approximation of the emissive integral term

$$J_b = B(T_s)\tau_s(\theta) + \int_{\tau_s(\theta)}^1 B[T(p)]\, d\tau(p, \theta), \tag{7}$$

and $\mathbf{G} = \mathbf{A}[\mathbf{J}_r]$ designates the linear approximation of the reflective integral term

$$J_r = -B[T_s]\tau_s(\theta) + \tau_s(\theta)\tau_s(\vartheta^*) \int_{\tau_s(\vartheta^*)}^1 B[T(p)]\tau^{-2}(p, \vartheta^*)\, d\tau\,(p, \vartheta^*). \tag{8}$$

For estimating ε (scalar), the normal estimate of the least squares solution is used—

$$\hat{\varepsilon} = 1 - \beta(\varepsilon)\mathbf{J}_r^{\mathrm{T}}[\mathbf{A}(\varepsilon)\mathbf{R}\mathbf{A}(\varepsilon)^{\mathrm{T}} + \mathbf{S}_{\xi}]^{-1}(\tilde{\mathbf{J}} - \mathbf{J}_b), \tag{9}$$

where

$$\beta(\varepsilon) = 1/\{\mathbf{J}_r^{\mathrm{T}}[\mathbf{A}(\varepsilon)\mathbf{R}\mathbf{A}(\varepsilon)^{\mathrm{T}} + \mathbf{S}]^{-1}\mathbf{J}_r\} \tag{10}$$

and superscripts T and -1 are transposition and inver-

sion operators, respectively. Under these conditions the estimate for $\mathbf{x}(p)$ has the following form:

$$\hat{\mathbf{x}} = \mathbf{R}\mathbf{A}(\varepsilon)^{\mathrm{T}}[\mathbf{A}(\varepsilon)\mathbf{R}\mathbf{A}(\varepsilon)]^{\mathrm{T}} + \mathbf{S}_{\xi})^{-1}\mathbf{f}(\varepsilon). \quad (11)$$

The solution of (1) was split into components because the functional derivative of radiance with respect to emissivity is much larger than the other derivatives. The error of the estimate (9) is

$$\delta\hat{\varepsilon} \approx -\beta(\varepsilon^*)\mathbf{J}_r[\mathbf{A}(\varepsilon^*)\mathbf{R}\mathbf{A}(\varepsilon^*)^{\mathrm{T}} + \mathbf{S}_{\xi}]^{-1}[\mathbf{A}(\varepsilon^*)\mathbf{x} + \boldsymbol{\xi}], \quad (12)$$

where ε^* is an unknown true value of emissivity. From (9) one then obtains

$$\overline{\delta\hat{\varepsilon}^2} \approx \beta(\varepsilon^*). \quad (13)$$

Equation (9) smoothes the influence of $(\mathbf{x}, \boldsymbol{\xi})$ with the statistical weight in the signal defined by the matrix $\mathbf{D}(\varepsilon) = [\mathbf{A}(\varepsilon)\mathbf{R}\mathbf{A}(\varepsilon)^{\mathrm{T}} + \mathbf{S}_{\xi}]$. Equations (9) and (11) are solved iteratively

$$\left.\begin{aligned}
\mathbf{X}^{(n)} &= \mathbf{X}^{(n-1)} + \mathbf{x}^{(n)} \\
\beta^{(n)} &= 1/\{\mathbf{J}_r[\mathbf{X}^{(n)}]^{\mathrm{T}}\mathbf{D}[\varepsilon^{(n)}]^{-1}\mathbf{J}_r[\mathbf{X}^{(n)}]\} \\
\varepsilon^{(n+1)} &= 1 - \beta^{(n)}\mathbf{J}_r[\mathbf{X}^{(n)}]^{\mathrm{T}}\mathbf{D}[\varepsilon^{(n)}]^{-1}\{\mathbf{J} - \mathbf{J}_b[\mathbf{X}^{(n)}]\} \\
\mathbf{J}[\mathbf{X}^{(n)}, \varepsilon^{(n+1)}] &= \mathbf{J}_b[\mathbf{X}^{(n)}] + [1 - \varepsilon^{(n+1)}]\mathbf{J}_r[\mathbf{X}^{(n)}] \\
\mathbf{f}^{(n+1)} &= \tilde{\mathbf{J}} - \mathbf{J}[\mathbf{X}^{(n)}, \varepsilon^{(n+1)}] \\
\mathbf{x}^{(n+1)} &= \mathbf{R}\mathbf{A}[\varepsilon^{(n+1)}]^{\mathrm{T}}\mathbf{D}(\varepsilon^{(n+1)})^{-1}\mathbf{f}^{(n+1)}
\end{aligned}\right\} \quad (14)$$

with the initial values $\mathbf{X}^{(0)} = \overline{\mathbf{X}}$, $\mathbf{x}^{(1)} = 0$, and $\varepsilon^{(1)} = \varepsilon_0$. The first guess emissivity ε_0 comes from already known information or can be constructed using (9) in the form

$$\varepsilon_0 = 1 - 1/[\mathbf{J}_r(\overline{\mathbf{X}})^{\mathrm{T}}\mathbf{S}_{\xi}^{-1}\mathbf{J}_r(\overline{\mathbf{X}})]\mathbf{J}_r(\overline{\mathbf{X}})^{\mathrm{T}}\mathbf{S}_{\xi}^{-1}[\mathbf{J} - \mathbf{J}_b(\overline{\mathbf{X}})].$$

It follows from (5)–(14) that the estimates of the temperature–humidity profiles are nonlinear functions of the emissivity estimate. Analyzing the final solution (14), it is possible to show that the variation in emissivity generates a bias and distorts the estimate of temperature–humidity parameters. The bias of the solution (14) is defined by the following relation:

$$\mathbf{b}(\varepsilon) = \overline{\frac{\partial\hat{\mathbf{x}}(\varepsilon)}{\partial\varepsilon}\delta\varepsilon} \approx \beta(\varepsilon)\mathbf{R}\mathbf{A}(\varepsilon)^{\mathrm{T}}\mathbf{D}(\varepsilon)^{-1}\mathbf{P}_{\mathbf{f}}(\varepsilon)\mathbf{G}\mathbf{R}\mathbf{A}(\varepsilon)^{\mathrm{T}}\mathbf{D}(\varepsilon)^{-1}\mathbf{J}_r, \quad (15)$$

where $\mathbf{P}_{\mathbf{f}}(\varepsilon) = \mathbf{E}_{\mathbf{f}} - \beta(\varepsilon)\mathbf{J}_r\mathbf{J}_r^{\mathrm{T}}\mathbf{D}(\varepsilon)^{-1}$ and $\mathbf{E}_{\mathbf{f}}$ is the identical matrix in the space of measurements. To provide stability in the solution with respect to emissivity uncertainties, an additional step of filtering the impact of emissivity on the estimates of the temperature–humidity parameters can be done as follows. Because the bias $\mathbf{b}(\varepsilon)$ describes a direction along which the emissivity disturbances propagate into the atmospheric part of the solution and where they accumulate, then it is sufficient to impose the orthogonality condition on the atmospheric part of the solution

$$(\hat{\mathbf{X}} - \overline{\mathbf{X}})^{\mathrm{T}}\mathbf{R}^{-1}\hat{\mathbf{b}}(\varepsilon) = 0, \quad (16)$$

which should be incorporated into the iterative schema (14). It is important to note, when solving (1) under the fixed emissivity value containing error $\delta\varepsilon$ in accordance with (5) and (11), the solution obtains a bias

$$\mathbf{b}_r = \delta\varepsilon\mathbf{R}\mathbf{A}(\varepsilon)^{\mathrm{T}}\mathbf{D}(\varepsilon)^{-1}\mathbf{J}_r. \quad (17)$$

The major difference between (14) and (16) is that the former is proportional to $\beta(\varepsilon) \approx (\delta\varepsilon)^2$, and the latter is proportional to $\delta\varepsilon$ (i.e., the accuracy of the solution is on average at least one order more accurate then the accuracy of the fixed emissivity solution with respect to the emissivity error).

To the formulation of the problem, the vector form for the estimate of the emissivity and the atmospheric solution bias is given as

$$\left.\begin{aligned}
\hat{\varepsilon} &= \mathbf{1} - [\boldsymbol{\Delta}_r^{\mathrm{T}}\mathbf{D}(\varepsilon)^{-1}\boldsymbol{\Delta}_r]^{-1}\boldsymbol{\Delta}_r^{\mathrm{T}}\mathbf{D}(\varepsilon)^{-1}(\tilde{\mathbf{J}} - \mathbf{J}_b) \\
\mathbf{S}_{\varepsilon} &= \overline{\delta\hat{\varepsilon}\delta\hat{\varepsilon}} \approx [\boldsymbol{\Delta}_r^{\mathrm{T}}\mathbf{D}(\varepsilon)^{-1}\boldsymbol{\Delta}_r]^{-1} \\
\hat{\mathbf{b}}(\varepsilon) &\approx \mathbf{R}\mathbf{A}(\varepsilon)^{\mathrm{T}}\mathbf{D}(\varepsilon)^{-1}\mathbf{P}_{\mathbf{f}}(\varepsilon)\mathbf{G}\mathbf{R}\mathbf{A}(\varepsilon)^{\mathrm{T}}\mathbf{D}(\varepsilon)^{-1}\boldsymbol{\Delta}_r\mathbf{S}_{\varepsilon}
\end{aligned}\right\}, \quad (18)$$

where $\mathbf{1}$ is understood as the vector, every component of which is equal to 1; $\boldsymbol{\Delta}_r = \partial\mathbf{J}/\partial\varepsilon$; and $\mathbf{P}_{\mathbf{f}}(\varepsilon) = \mathbf{E}_{\mathbf{f}} - \boldsymbol{\Delta}_r\mathbf{S}_{\varepsilon}\boldsymbol{\Delta}_r^{T}\mathbf{D}(\varepsilon)^{-1}$.

3. Application of the surface emissivity correction to MODIS Airborne Simulator (MAS) data

Application of the proposed approach to measurements from a multispectral radiometer with high spatial resolution [moderate resolution imaging spectroradiometer (MODIS) Airborne Simulator (MAS; King at al. 1996)] is presented in this section. MAS data were chosen because the high spatial resolution (about 50 m) allows the spatial variations of the atmospheric profiles in adjacent fields of view to be disregarded, and spatial variations of spectral measurements will be explained mainly by changes in the surface temperature and emissivity from FOV to FOV. The influence of radiometric noise can be diminished by the spatial smoothing of measurements; 10 × 10 fields of view were averaged (representing 500 m × 500 m areas). The relevant MAS channels and their measurement accuracies are presented in Table 1. After spatial averaging, noise is reduced by an order of magnitude so the data have a nominal accuracy of better than 0.2 K in all channels.

The MAS measurements are used to retrieve estimates of the surface emissivity (from 4.52 to 5.28 μm and 8.60 to 12.88 μm), the surface temperature, and the atmospheric temperature and humidity profiles, using the model [(1)] and the estimates [(2)–(5)]. The emissivity spectrum partition used is based upon results of direct emissivity measurements from Salisbury et al. (1992; 1994) and Labed and Stoll (1991a). The solution was constrained so that the emissivity value $\hat{\varepsilon} \leq 0.98$.

TABLE 1. MAS channels used in this study.

MAS channel	Central wavelength [μm]	Equivalent noise for single FOV measurement for 300 K target (K)	Main purpose: *T* temperature *Q* moisture
36	4.52	0.28	Midlevel *T*
37	4.67	0.14	Low-level *T*
38	4.82	0.13	Low-level *T*
39	4.97	0.12	Low-level *T, Q*
40	5.12	0.14	Low-level *T, Q*
41	5.28	0.18	Midlevel *T, Q*
42	8.60	0.14	Surface *T*
44	10.55	0.09	Surface *T*
45	11.02	0.10	Surface *T*
46	11.96	0.19	Surface *T, Q*
47	12.88	0.46	Surface *T, Q*
48	13.23	0.49	Low-level *T*
49	13.72	1.32	Midlevel *T*
50	14.17	2.00	Upper-level *T*

The test dataset came from an ER-2 flight over the Cloud and Radiation Testbed (CART) site in Oklahoma (36.61°N, 97.49°W) on 13 April 1996 from 1825 to 1835 UTC. The full-resolution measurement matrix is 716 pixels per scanning line by 2991 lines, where a scan line extends about 37 km. Total field of view is 85.9°. After averaging, the size of the processed image is 71 $\times$ 299 elements (angle size of the averaged block is 1.2°). The image is cloud free. Figure 1 shows the mean surface and atmospheric conditions, demonstrated by the alongtrack average of the measurements as a function of scan angle. The scene is inhomogeneous, showing considerable irregularities in the surface properties and a temperature gradient along the scan line. Land cover conditions include vegetated and nonvegetated soil, dry and wet soil, and some lakes and rivers.

A radiosonde launched from the CART site at 1731 UTC was used as a first guess for the retrieval algorithm. Using the radiosonde profile as the first guess in the algorithm is an important feature of this study, because it allows

1) minimization of the influence of the first guess on the final estimate,
2) estimatation of the minimum effect of the emissivity on the estimate of the temperature–humidity profile, and
3) evaluation of the mutual influence of different physical components in the estimates (9) and (11).

The time difference between the MAS flight data and the radiosonde is 1 h. The radiosonde temperature–humidity profiles are presented in Fig. 2. Note that the troposphere is quite warm and dry. The profiles show a strong inversion in the lower troposphere.

Statistics of estimates for the surface emissivity in the shortwave (4.52–5.28 μm—ε_1) and longwave (8.60–12.88 μm—ε_2) and the surface temperature T_s are shown in Table 2. The surface temperatures derived from the MAS radiances ranged from 295.3 to 317.7 K;

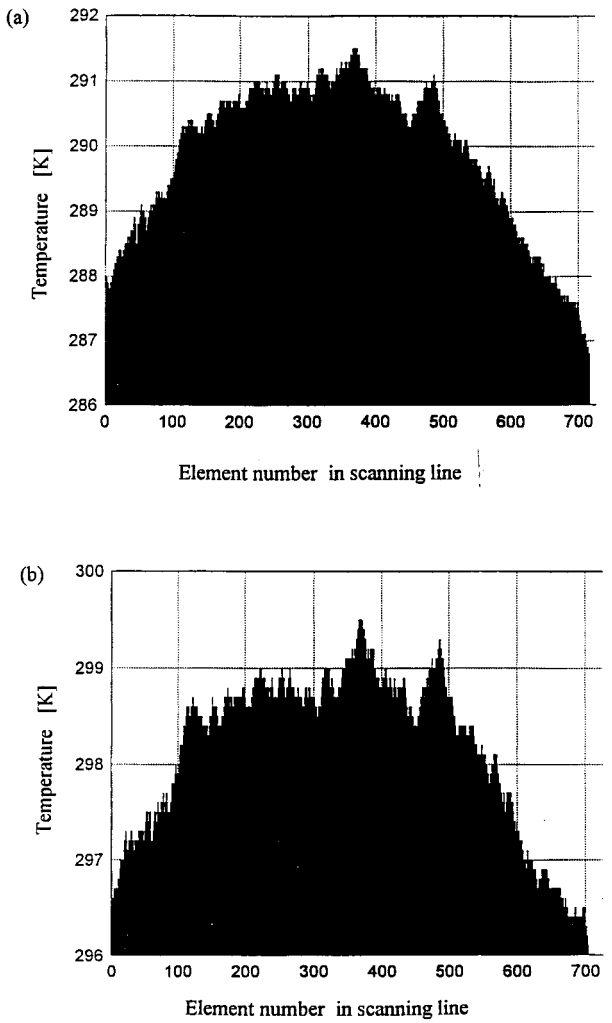

FIG. 1. The averaged measurement distribution for each element of the scan line: (a) channel 37 (4.67 μm), (b) channel 42 (8.60 μm).

the corresponding range for the shortwave emissivities is 0.897 to 0.980, while the longwave emissivities span from 0.951 to 0.980. The emissivity shows considerable variation from short- to longwave and from one FOV to another, thus showing that an assumption of constant surface emissivity is a very rigid restriction in modeling real land covers.

Figure 3 shows the estimated emissivity as a function of a block number n in the scanning line, where the scan angle $\theta_n \approx 1.2|n - 36|°$. Emissivity decreases smoothly with increasing scan angle (angle of incidence). It should be noted that the emissivity statistics obtained do not refer to any specific surface cover type and these characteristics are in good agreement with the general statements of the reflection theory (e.g., Hapke 1993) and with direct laboratory and field measurements (Schmugge et al. 1991; Labed and Stoll 1991b). The shortwave emissivity distribution is found to be asymmetrical and the value at nadir (maximum) is close to

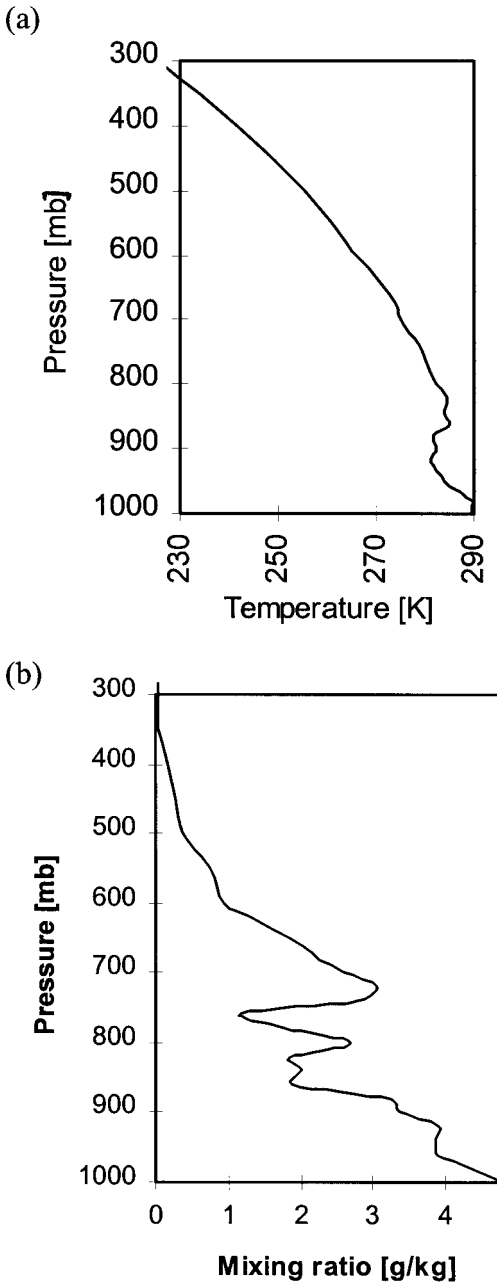

FIG. 2. Radiosonde (a) temperature and (b) humidity profiles observed at the CART site at 1731 UTC on 13 Apr 1996.

TABLE 2. Statistics of estimates of surface parameters.

	Mean	Min	Max	Std dev
ε_1	0.959	0.897	0.980	0.013
ε_2	0.970	0.951	0.980	0.005
T_s	307.7	295.3	317.3	2.4

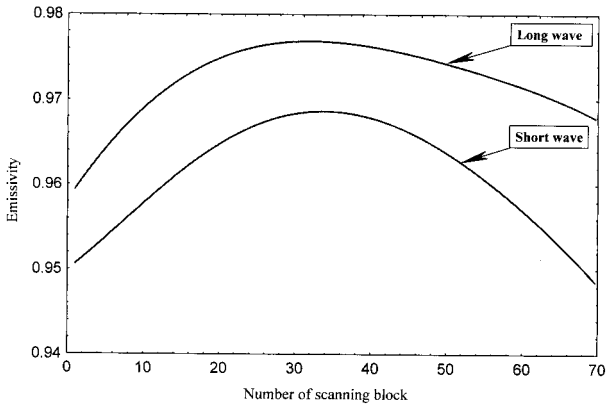

FIG. 3. Estimates of the emissivity distribution in two spectral bands as a function of scan block number (scan angle): shortwave ε_1 4.52–5.28 μm (lower line) and longwave ε_2 8.60–12.88 μm (upper line). The scanning block represents 10 samples along a scan line.

the maximum constraint of emissivity. For comparison, the longwave emissivity distribution is symmetrical and the value at nadir is substantially less than the emmissivity limit. The asymmetry of the shortwave emissivity distribution can be explained by the difference in the land cover on the left and right edges of the scene. To some extent Fig. 3 indicates the modeling accuracy for short-and longwave bands and the difference in the short- and longwave measurements (the information contents with respect to the emissivity). In the shortwave band the presence of the reflected solar radiance is ignored, which increases the emissivity estimate and the asymmetry. The information content of the measurements also is different; Table 1 shows that there are ''atmospheric'' channels in the shortwave band, and mostly ''surface'' channels in the longwave band. That difference is confirmed quantitatively by Fig. 4, which shows the spectral distribution of the reflective contribution $J_r/(dB[T]/dT)_{\bar{T}:B[\bar{T}]=\bar{J}}$ to the measurement. The reflective contribution for the longwave band is approx-

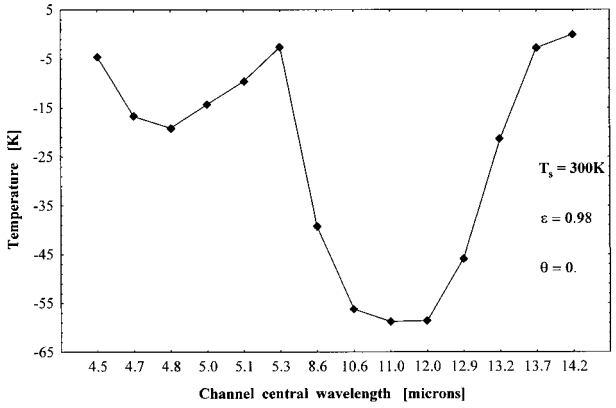

FIG. 4. An example of spectral distribution of $J_r/(dB[T]/dT)_{\bar{T}:B[\bar{T}]=\bar{J}}$, which defines the reflective contribution to the measurement.

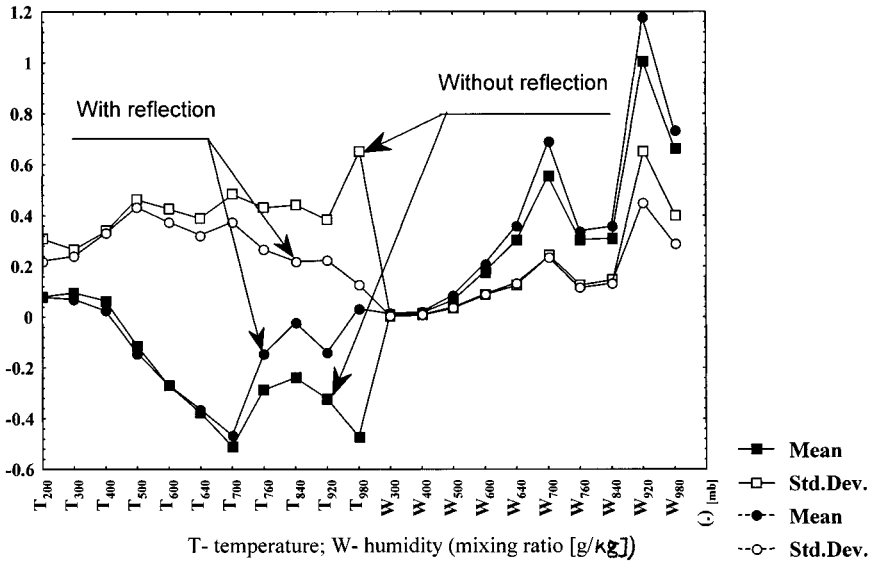

FIG. 5. Temperature and mixing ratio profile statistics (mean and standard deviation of first guess adjustment, retrieval minus guess) for the two models (with and without surface reflection).

imately one order of magnitude larger than for the shortwave band.

Figure 5 shows the atmospheric profile statistics (mean and standard deviation) of the derived solutions with surface reflection using (9)–(18) and without surface reflection (emissivity equal to 1). The assumption of a blackbody surface considerably distorts the solution in the lower troposphere, even when the first guess was very close to the real temperature–humidity vertical distribution. In the RTE model with reflection there is less emission from the warm surface and more emission of the cooler atmosphere because of the reflection. This result implies that the magnitude of variation of the humidity mixing ratio estimate for a reflecting surface should be larger than for a black surface, as is illustrated in Fig. 5. As can be seen, the one major feature of the influence of the emissivity estimate on the estimate of the vertical temperature–humidity profile is the reduction of variance values with the increasing value of mean moisture contents. In a trivial case the introduction of an additional parameter into the measurement model would result only in absorption of a part of the measurement signal by the new parameter and a corresponding reduction of obtained amplitudes of estimates of other components of the solution.

Figure 6 shows the spatial distribution in the observed scene of the Normalized Difference Vegetation Index (NDVI) along with the surface temperature estimate from the model with reflection and without reflection (emissivity equal to 1). The complex structure of the observed scene is illustrated in Fig. 6a [the image scene in terms of NDVI (see, e.g., Tucker 1979), which was defined in the experiment by the relation NDVI = $(I_{0.87} - I_{0.66})/(I_{0.87} + I_{0.66})$ (dimensionless), where $I_{0.66}$ and $I_{0.87}$ are measurements in visible channels 0.66 μm and 0.87 μm, respectively]. The NDVI parameter commonly is used to discriminate surface conditions: the higher NDVI value corresponds to a higher spatial density of vegetation (Curran 1980; Justice et al. 1985). Analysis of Fig. 6a reveals that the image could be characterized as an anisotropic spatial distribution of a mixture of different surface types. Open water has a negative value of NDVI. Figure 6a represents the independent information with respect to estimations of the spatial distribution of surface temperature. Figure 6b corresponds to the solution of the RTE model with reflection. Note the considerable variations in surface temperature within the scene. In comparing Figs. 6a and 6b, it can be seen that maxima of surface temperature correspond mostly to the dry nonvegetated surfaces. Figure 6c shows the spatial distribution of differences in surface temperature estimates from Fig. 6b and without reflection (emissivity equal to 1). Figure 6c reveals that the surface temperature estimate for the RTE model with a fixed emissivity value strongly depends on the angle of incidence. The differences range from 1 to 4 K. The mean difference is 2.2 K. The difference shows considerable variation from one FOV to another and directly reflects the spatial–angle distribution of the emissivity estimate. Figure 7 shows the surface temperature relationship to the NDVI parameter: a statistically significant negative correlation ($r = -0.78$) is obtained for temperature versus NDVI. The increasing NDVI corresponds to the increasing vegetation density, which, in turn, decreases the temperature by evaporation.

Figure 8 shows the temperature distribution of a subsample of cases with an overheated surface $\{T_s : T_s \geq \overline{T}_s + 2\sigma_{T_s}\}$ and illustrates another important physical feature: overheated cases have low values of NDVI, and surface temperature estimates do not depend on NDVI.

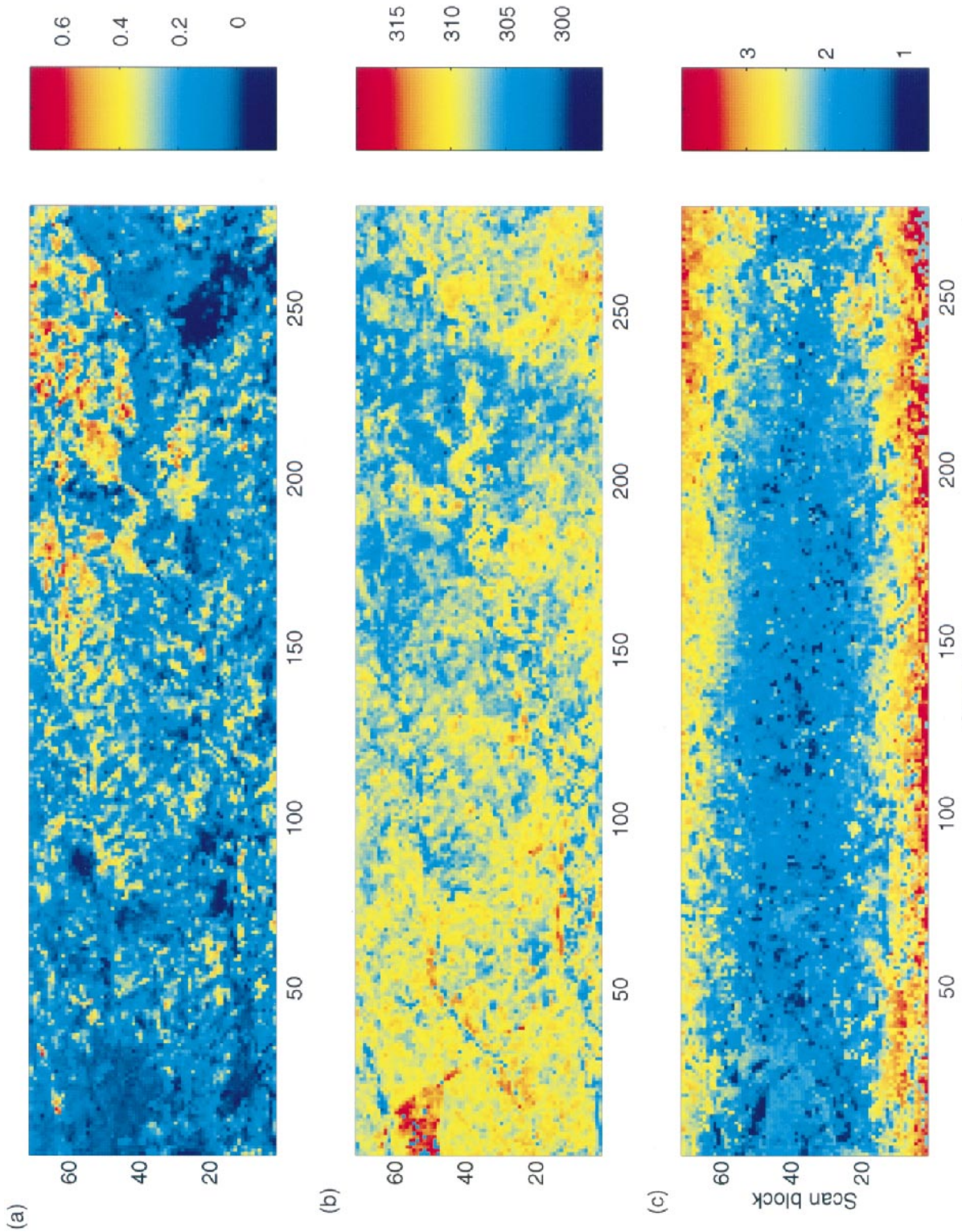

FIG. 6. (a) The image of an observed scene in terms of NDVI, and composite images of surface temperature estimates for two surface models: (b) with reflection and (c) difference of estimates with and without reflection.

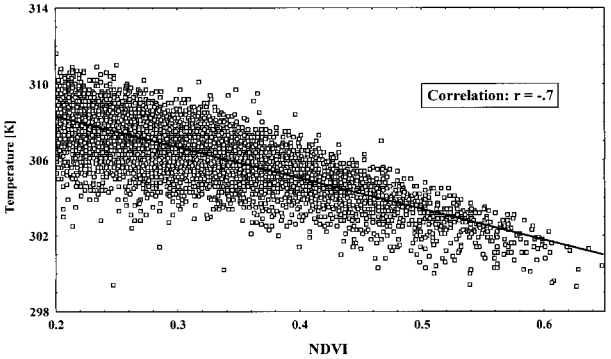

FIG. 7. Scatterplot of surface temperature estimates vs measurements in the visible spectral band in terms of NDVI (7542 cases with NDVI > 0.2).

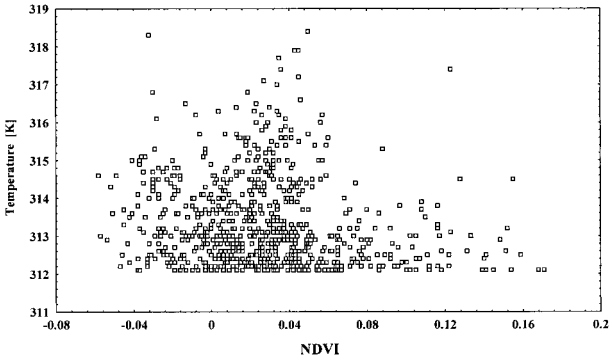

FIG. 8. Scatterplot of surface temperature estimates vs NDVI for a subsample of 761 cases with an overheated surface.

The low NDVI value means that the subsample corresponds to conditions consistent with a nonvegetated surface. Figures 6–8 demonstrate that the surface temperature estimates obtained for the model with reflection are physically grounded.

Figure 9 shows the spatial distribution of (a) the emissivity estimate for the band 10.6–13.2 μm, (b) the humidity mixing ratio at 920 hPa from the model with reflection, and (c) the differences of the humidity mixing ratio estimate with reflection minus that without reflection (emissivity equal to 1). In Fig. 9, note the considerable variations of the emissivity and moisture estimates within the scene. The humidity at 920 hPa exhibits substantial variation, with strong gradients along the track. Values range from 0.536 to 1.790 g kg^{-1} in the scene. The humidity patterns are very different from those of the surface temperature. The radiosonde location at the CART site corresponds to scan block 28 and scan line 128. A comparison of Figs. 9b and 9c reveals that the moisture estimate for the RTE model with a fixed emissivity shows a strong dependence on the angle of incidence. The differences range from -2 to 2 g kg^{-1}. The mean difference is 0.2 g kg^{-1}. The difference reflects the spatial–angle distribution of the emissivity estimate presented in Fig. 9a. It is important to note that, in the case of overheated surfaces, the moisture estimate in the model with reflection is more stable. Figure 10 clearly demonstrates that the solution under fixed emissivity has on average a nonuniform spatial distribution along the scan line, that is, the estimate depends on the measurement geometry. The subsample of estimates from lines 50–240, which corresponds to comparatively homogeneous surface conditions, was used for generating Fig. 10. A comparison of panels (a) and (b) in Fig. 10 shows the stability of the moisture estimate from the model with reflection with respect to the measurement geometry and variations of surface conditions.

A measure of the stability of the solutions with and without surface reflection also can be found in the horizontal variation of the solution at any level in the atmosphere. Its variation is influenced largely by the emissivity error estimate and measurement noise. This quantity can be measured with the second spatial derivative: a smoother second derivative is a more physically realistic result, since the spatial variations of atmospheric parameters at adjacent FOVs are negligibly small in comparison with spatial variations of the surface parameters.

The finite difference approximation of the second derivative on the uniform grid with space increment Δ has the form

$$\frac{\partial^2 \mathbf{f}(x, y)}{\partial x^2} \approx \mathbf{f}''_{1,0} = \frac{\mathbf{f}_{1,0} + \mathbf{f}_{-1,0} - 2\mathbf{f}_{0,0}}{2\Delta^2},$$

$$\frac{\partial^2 \mathbf{f}(x, y)}{\partial y^2} \approx \mathbf{f}''_{0,1} = \frac{\mathbf{f}_{0,1} + \mathbf{f}_{0,-1} - 2\mathbf{f}_{0,0}}{2\Delta^2},$$

where $\mathbf{f}_{0,0} = \mathbf{f}(x, y)$, $\mathbf{f}_{\pm 1,0} = \mathbf{f}(x \pm \Delta, y)$, $\mathbf{f}_{0,\pm 1} = \mathbf{f}(x, y \pm \Delta)$. In the same way, the derivatives in diagonal directions can be defined as

$$\mathbf{f}''_{1,1} = \frac{\mathbf{f}_{1,1} + \mathbf{f}_{-1,-1} - 2\mathbf{f}_{0,0}}{4\Delta^2} \quad \text{and}$$

$$\mathbf{f}''_{1,-1} = \frac{\mathbf{f}_{1,-1} + \mathbf{f}_{-1,1} - 2\mathbf{f}_{0,0}}{4\Delta^2},$$

where $\mathbf{f}_{\pm 1,\pm 1} = \mathbf{f}(x \pm \Delta, y \pm \Delta)$. Then by summing up components $\mathbf{f}''_{i,j}$ one obtains the expression

$$\sum_{i,j} \mathbf{f}''_{i,j} = \frac{1}{4\Delta^2}(2\mathbf{f}_{0,1} + 2\mathbf{f}_{0,-1} + 2\mathbf{f}_{1,0} + 2\mathbf{f}_{-1,0} + \mathbf{f}_{1,1} + \mathbf{f}_{-1,-1} + \mathbf{f}_{-1,1} + \mathbf{f}_{1,-1} - 12\mathbf{f}_{0,0}).$$

Statistics of this function describe the spatial ''roughness'' of the observed field of measurement. As shown, the spatial roughness of the atmospheric parameter estimate is a function of spatial roughness of the surface parameters, and the variance of roughness of an atmospheric parameter estimate is the measure of accuracy for estimates of surface parameters: the less variance, the more accurate the surface parameter estimate is. The standard deviation of the function $\Sigma_{i,j} \mathbf{f}''_{i,j}$ of the

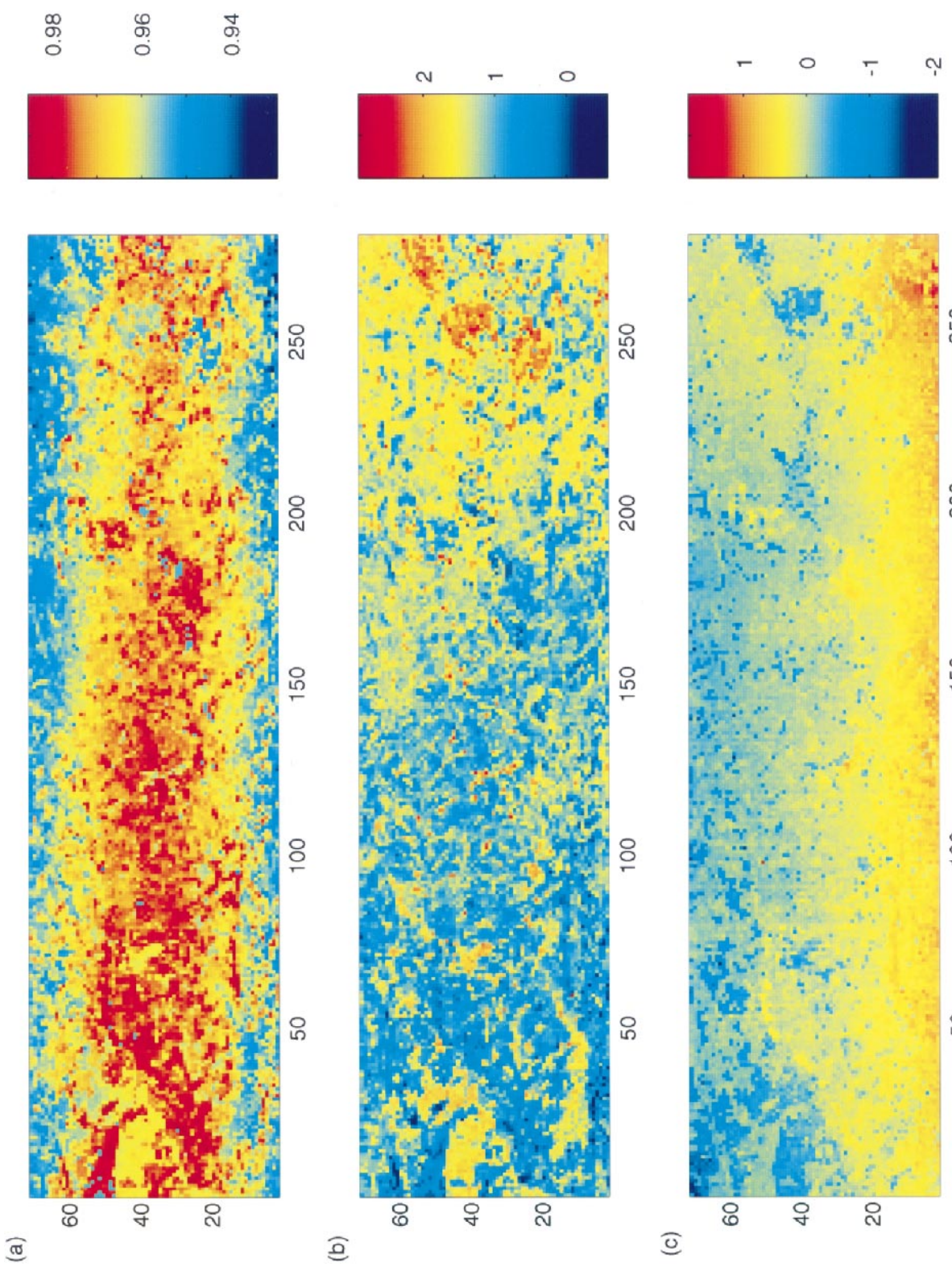

FIG. 9. (a) Composite images of the emissivity estimate for the band 10.6–13.2 μm, moisture estimates (g kg^{-1}) at the level 920 hPa for two surface models: (b) with reflection and (c) difference of estimates with reflection minus those without reflection.

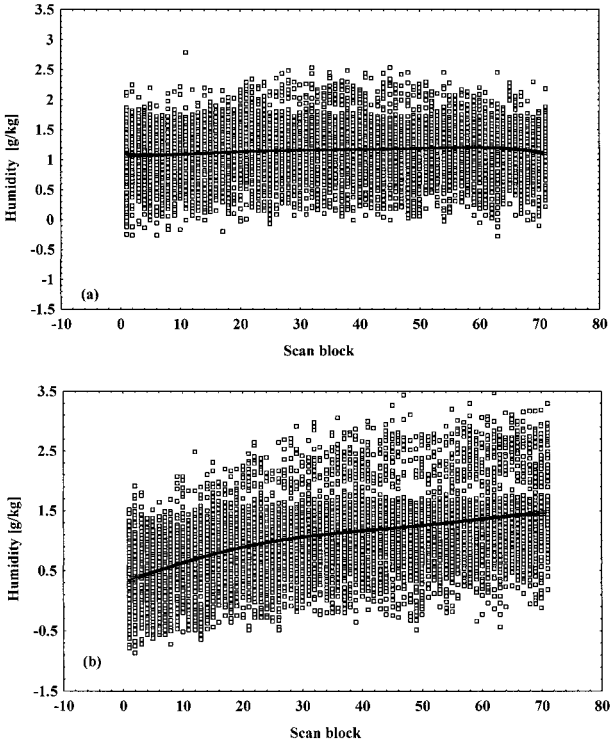

FIG. 10. Estimates of humidity mixing ratio at 920 hPa for two models: (a) with reflection and (b) without reflection as a function of scan block number for a homogeneous subsample of surface conditions.

second spatial derivatives of the temperature and moisture solution for a given level with and without surface reflection is shown in Fig. 11. As follows from data in Fig. 11, the solution with surface reflection is much smoother and hence more correct than the solution without surface reflection is. Note that the measure used for the spatial smoothness of the solution directly relates to thermodynamical properties of the atmosphere: the spatially smoother solution better satisfies the equation of continuity.

4. Conclusions

The effects of reflection in the surface–atmosphere system were incorporated into a solution of the inverse problem of atmospheric meteorological remote sensing from space. The model of infrared spectral measurements based upon the radiative transfer equation with variable surface emissivity was formulated. The surface reflection in the model is described by the hemispherical directional effective emissivity under a given effective angle of incidence. The inverse problem for estimating the surface emissivity (shortwave and longwave), surface temperature, and vertical profiles of temperature and humidity was formulated. The emissivity estimate was considered as a parameter of solution. The algorithm for solution was derived.

The proposed algorithm was applied to the multispectral measurements of the airborne MAS instrument from the Subsonic Aircraft: Contrail and Cloud Effects Special Study (SUCCESS) campaign. The measured data described the spatial distribution of the outgoing radiance from land cover with a complex structure. These retrieved temperature and moisture profiles were compared with results from processing with a ''black surface.'' It is shown that including the surface emissivity as a parameter into the solution of the inverse problem changes the properties of meteorological com-

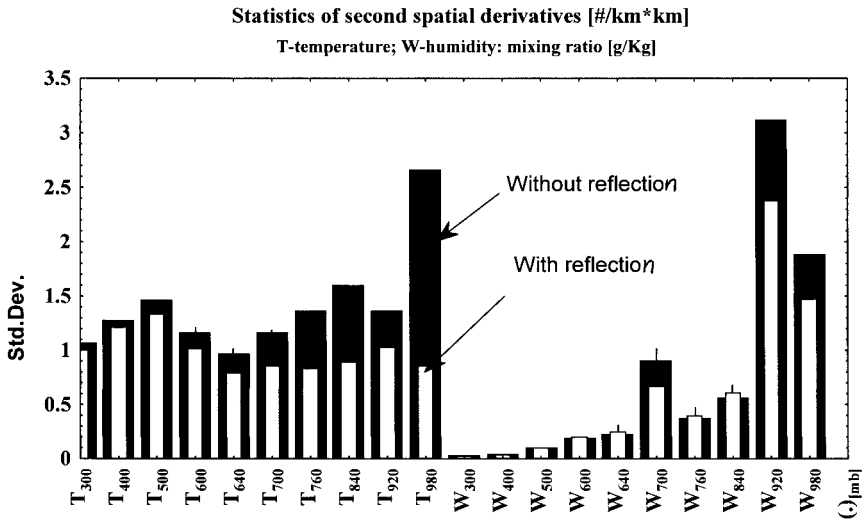

FIG. 11. Stability of the solution for the two algorithms (with and without surface reflection) as measured by the standard deviation of the second derivative of the horizontal variation of temperature or mixing ratio at a given level of the atmosphere. Smaller values are more stable and hence better depict the actual atmospheric state.

ponents of the solution substantially and for the better. Strong correlation (less than -0.75) between derived surface temperature and the independent vegetation index was found. The solution that corresponds to the RTE model with reflection of infrared radiation from the earth's surface produced smoother, more physical atmospheric variations of temperature and moisture. The procedure for solving the inverse problem is effective and reliable.

The results demonstrate the importance of accounting for the effect of reflection in interpreting IR measurements from the National Oceanic and Atmospheric Administration (NOAA) and GOES operational meteorological satellites. For the GOES and NOAA operational soundings, there are several implications. It was shown with 500-m MAS data that

- the surface emissivity is one of the strongest-varying parameters in the RTE for infrared remote sensing,
- an assumption of fixed emissivity is not effective for retrieving temperature and moisture profiles because the surface emissivity is a function of the angle of incidence and the composite cover of the surface, and
- emissivity errors distort the atmospheric parameters, primarily in the lower troposphere.

These findings mean that including the influence of the earth's surface emissivity on tropospheric temperature and moisture profiles should improve the accuracy of the soundings 1) on the edges of the GOES and NOAA scenes, 2) over land surface, and 3) in warm, humid atmospheric conditions. Estimates of total precipitable water vapor could be expected to improve substantially.

Acknowledgments. The authors thank the Space Science and Engineering Center (Madison, Wisconsin) for all the resources to which they had access. They thank Mr. Christopher Moeller for providing the MAS measurements and Mr. Harold Woolf for assistance with radiative transfer calculations. Partial support for this study was provided by NAS5-31367 and NA67EC0100.

REFERENCES

Beckmann, P., and A. Spizzchino, 1963: *The Scattering of Electromagnetic Waves from Rough Surfaces.* Pergamon Press, 503 pp.

Curran, P. J., 1980: Multispectral remote sensing of vegetation amount. *Progr. Phys. Geogr.,* **4,** 315–341.

Hapke, B., 1993: *Theory of Reflectance and Emittence Spectroscopy (Topics in Remote Sensing, 3).* Cambridge University Press, 455 pp.

Hayden, C. M., 1988: GOES-VAS simultaneous temperature–moisture retrieval algorithm. *J. Appl. Meteor.,* **27,** 705–733.

Justice, C. O., J. R. Townshend, B. N. Holben, and C. J. Tucker, 1985: Analysis of the phenology of global vegetation using meteorological satellite data. *Int. J. Remote Sens.,* **6,** 1271–1318.

King, M. D., and Coauthors, 1996: Airborne scanning spectrometer for remote sensing of cloud, aerosol, water vapor, and surface properties. *J. Atmos. Oceanic Technol.,* **13,** 777–793.

Labed, J., and M. P. Stoll, 1991a: Spatial variability of land surface emissivity in the thermal infrared band: Spectral signature and effective surface temperature. *Remote Sens. Environ.,* **38,** 1–17.

——, and ——, 1991b: Angular variation of land surface emissivity in the thermal infrared: Laboratory investigations on bare soils. *Int. J. Remote Sens.,* **12,** 2299–2310.

Nicodemus, F. E., 1965: Directional reflectance and emissivity of an opaque surface. *Appl. Opt.,* **4,** 767–773.

Rao, C. R., 1965: *Linear Statistical Inference and its Applications.* John Wiley and Sons, 522 pp.

Salisbury, J., W. D'Aria, and M. Dana, 1992: Emissivity of terrestrial materials in the 8–12 μm atmospheric window. *Remote Sens. Environ.,* **42,** 83–106.

——, ——, and ——, 1994: Emissivity of terrestrial materials in the 3–5 μm atmospheric window. *Remote Sens. Environ.,* **47,** 345–361.

Schmugge, T. J., F. Becker, and Z. Li, 1991: Spectral emissivity variations observed in airborne surface temperature measurements. *Remote Sens. Environ.,* **13,** 95–104.

Tikhonov, A. N., and V. Ya. Arsenin, 1977: *Solutions of Ill-Posed Problems.* Winston, 258 pp.

Tucker, C. J., 1979: Red and photographic infrared linear combinations for monitoring vegetation. *Remote Sens. Environ.,* **8,** 127–150.